A Projection Method for Incompressible Viscous Flow on Moving Quadrilateral Grids[1]

David P. Trebotich[*] and Phillip Colella[†]

[*]*Department of Mechanical Engineering, University of California, Berkeley, California 94720; and*
[†]*Applied Numerical Algorithms Group, Lawrence Berkeley National Laboratory, Berkeley, California 94720*
E-mail: treb@me.berkeley.edu

We present a second-order accurate projection method for numerical solution of the incompressible Navier–Stokes equations on moving quadrilateral grids. Our approach is a generalization of the Bell–Colella–Glaz (BCG) predictor–corrector method for incompressible flow. Irregular geometry is represented in terms of a moving, body-fitted cylindrical coordinate system. Mapped coordinates are used to smoothly transform in both time and space the moving domain onto a logically rectangular domain which is fixed in time. To treat the time dependence and inhomogeneities in the incompressibility constraint introduced by the presence of deforming boundaries, we introduce a nontrivial splitting of the velocity field into vortical and potential components to eliminate the inhomogeneous terms in the constraint and a generalization of the BCG algorithm to treat time-dependent constraints. The method is second-order accurate in space and time, has a time step constraint determined by the advective CFL condition, and requires the solution of well-behaved linear systems amenable to the use of fast iterative methods. We demonstrate the method on the specific example of viscous incompressible flow in an axisymmetric deforming tube. © 2001 Academic Press

Key Words: projection methods; deformable domains; incompressible flow; Navier–Stokes equations.

1. INTRODUCTION

The incompressible Navier–Stokes equations are a combination of evolution equations and constraints resulting from the incompressibility condition:

$$\mathbf{u}_t + \operatorname{div}(\mathbf{u} \otimes \mathbf{u}) = -\operatorname{grad}(p) + \nu \Delta \mathbf{u}$$
$$\operatorname{div}(\mathbf{u}) = 0. \tag{1}$$

As such, the formulation of appropriate time-discretization methods is more subtle than is the case for evolution equations. To address this issue, Chorin [10] introduced projection methods, based on the Hodge decomposition of any vector field into a divergence-free part and a gradient of a scalar field. Projection methods are fractional step methods for which an intermediate velocity is computed that does not necessarily satisfy the incompressibility constraint. Then this velocity is corrected so that it satisfies the constraint. More recently, Bell, Colella, and Glaz (BCG) [6] introduced a predictor–corrector method based on Chorin's ideas. Some of the key advantages of their method are that the advective terms can be treated using explicit high-resolution finite difference methods for hyperbolic PDEs and that only linear systems, coming from standard discretizations of second-order elliptic and parabolic PDEs which are amenable to solution using fast iterative methods such as the multigrid method, must be solved. This leads to a method that is second-order accurate in space and time. It has a stability constraint on the time step due only to the CFL condition for the advection terms and provides a robust treatment of underresolved gradients in the Euler limit. This method has been the basis for the extensive development of new algorithms for the treatment of a variety of low Mach number flow problems [1, 2, 8, 9, 13, 21, 23, 25, 27, 30].

The purpose of this paper is to present the extension of the BCG algorithm to the case of moving deformable boundaries. The principal difference is that the boundary conditions for the divergence-free constraint become both inhomogeneous and time-dependent. There have been a number of previous methods which model deformable boundaries [15, 24, 28], but none combine the accuracy, efficiency, and robustness of the BCG approach. We attack this problem using three ideas. First, we address the deformable nonrectangular domain with a moving, mapped grid. Second, we eliminate the inhomogeneity in the constraint equation by performing a nontrivial Hodge splitting of the velocity field into a potential component that carries the inhomogeneities in the boundary conditions for the divergence constraint and a vortical component that satisfies an evolution equation with time-dependent, but homogeneous, constraints. The third idea is a new time discretization for time-dependent, constrained systems. The end result is a method that retains the advantages of the BCG algorithm, but for the more general case of flows in deforming domains.

Preliminary versions of these results appear in [14, 31].

2. PHYSICAL PROBLEM

We consider the problem of flow in an axisymmetric, flexible tube (see Fig. 1). The dashed top boundary of the figure is the centerline, or axis of symmetry, of the tube where $r = 0$. There is flow into the tube at the left boundary where the classic Poiseuille velocity profile for viscous flow in pipes is prescribed. The wall of the tube is the bottom boundary, $r = R(z, t)$. This infinitely thin solid wall boundary is allowed to move in the middle section of the tube with a prescribed velocity. The inlet and outlet remain fixed.
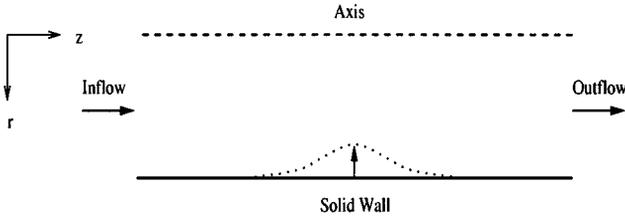
FIG. 1.   Flow through an axisymmetric deforming tube.

Mapped coordinates.   We address the issue of domain deformability with moving, mapped coordinates. We define a continuous mapping from an abstract fixed coordinate system, $\boldsymbol{\xi} = (\xi, \eta)$, to real axisymmetric coordinates which are time-dependent, $\mathbf{x}(t) = (r(t), z(t))$:

$$\mathbf{x} = \chi(\boldsymbol{\xi}, t). \tag{2}$$

We then define divergence, gradient, and Laplacian operators in mapped coordinates as

$$\mathrm{div}(\mathbf{u}) = \nabla \cdot \mathbf{u} = J^{-1} \nabla_\xi \cdot (J\mathbf{F}^{-1}\mathbf{u})$$

$$\mathrm{grad}(p) = \nabla p = \mathbf{F}^{-T} \nabla_\xi p \tag{3}$$

$$\Delta \mathbf{u} = \nabla \cdot (\nabla \mathbf{u}) = J^{-1} \nabla_\xi \cdot (J\mathbf{F}^{-1}\mathbf{F}^{-T} \nabla_\xi \mathbf{u}),$$

where $\mathbf{u}$ and p are velocity and pressure, respectively, and J is the determinant of $\mathbf{F} = \frac{\partial x}{\partial \xi}$. The inverse transformation matrix, $\mathbf{F}^{-1}$, is defined as

$$\mathbf{F}^{-1} = gJ^{-1} \begin{bmatrix} z_n & -r_n \\ -z_\xi & r_\xi \end{bmatrix}, \tag{4}$$

where $g = 2\pi r$. The appropriate volume weighting of the inverse transformation is derived from the unrestricted three-dimensional definition of the transformation matrix. To understand this quantity discretely, it must be placed into the correct context—namely, transformation of a vector in real coordinates to one in mapped coordinates. This will be discussed as needed in the details of the algorithm.

The incompressible Navier–Stokes equations (1) transform into mapped coordinates as

$$\mathbf{u}_t|_\xi + \mathrm{div}[(\mathbf{u} - \mathbf{s}) \otimes \mathbf{u}] = -\mathrm{grad}(p) + \nu\Delta\mathbf{u}$$

$$\mathrm{div}(\mathbf{u}) = 0, \tag{5}$$

where $\mathbf{s} = \frac{\partial \chi}{\partial t}$ is the velocity of the moving coordinate system and ν is the kinematic viscosity.

The boundary conditions for viscous incompressible flow in an axisymmetric deforming tube are

(1) along the axis of symmetry (no flow)

$$\mathbf{u} \cdot \mathbf{n} = 0,$$

(2) at the solid wall (prescribed boundary motion)

$$\mathbf{u} = \mathbf{u}_b,$$

(3) at inflow (prescribed Poiseuille flow)

$$u = 0$$
$$v = 2(1 - r^2),$$

(4) at outflow

$$\frac{\partial \mathbf{u}}{\partial z} = 0. \tag{6}$$

In addition, we will specify a Dirichlet boundary condition on p at outflow. The exact form of this pressure boundary condition is deferred for later discussion.

Split-velocity formulation.   We decompose the solution to (1) into two components: $\mathbf{u}_v$, which carries the velocity field induced by the vorticity, and $\mathbf{u}_p$, a nontrivial potential flow field induced by the deforming boundary:

$$\mathbf{u} = \mathbf{u}_v + \mathbf{u}_p$$
$$\text{div}(\mathbf{u}_v) = 0 \tag{7}$$
$$\mathbf{u}_p = \text{grad}(\phi).$$

Here, ϕ is the solution to Laplace's equation, $\Delta\phi = 0$, with normal boundary conditions (see Fig. 1 for geometry) given by

(1) along axis of symmetry (no flow)

$$\mathbf{u}_p \cdot \mathbf{n} = 0, \tag{8}$$

(2) at the solid wall (prescribed boundary motion)

$$\mathbf{u}_p \cdot \mathbf{n} = \mathbf{u}_b \cdot \mathbf{n}, \tag{9}$$

(3) at inflow (constant mean flow)

$$\mathbf{u}_p \cdot \mathbf{n} = v_{in}, \tag{10}$$

(4) at outflow (conservation of mass, 1D mean flow)

$$\mathbf{u}_p \cdot \mathbf{n} = v_{out}, \tag{11}$$

where v_{out} is the one-dimensional solution obtained from conservation of mass for flow in a flexible tube with fixed inlet and outlet:

$$\int_0^{R_{out}} 2\pi r (\mathbf{u}_p \cdot \mathbf{n})\, dr + \int_0^{R_{in}} 2\pi r (\mathbf{u}_p \cdot \mathbf{n})\, dr + \int_0^{L_{wall}} 2\pi R(l)(\mathbf{u}_p \cdot \mathbf{n})\, dl = 0. \tag{12}$$

This leads to the equation of motion for $\mathbf{u}_v$,

$$\left.\frac{\partial \mathbf{u}_v}{\partial t}\right|_\xi = \mathcal{F}(\mathbf{u}_v, \mathbf{u}_p) - \mathrm{grad}(\pi)$$

$$\mathrm{div}(\mathbf{u}_v) = 0, \tag{13}$$

where

$$\mathcal{F}(\mathbf{u}_v, \mathbf{u}_p) = -\mathbf{A}_s(\mathbf{u}_v, \mathbf{u}_p) + \nu \Delta \mathbf{u}$$

$$\mathbf{A}_s(\mathbf{u}_v, \mathbf{u}_p) = \mathbf{u}_v \cdot \nabla \mathbf{u}_p + (\mathbf{u} - \mathbf{s}) \cdot \nabla \mathbf{u}_v \tag{14}$$

$$\pi = \left.\frac{\partial \phi}{\partial t}\right|_x + \frac{|\mathbf{u}_p|^2}{2} + p.$$

The advantage of this formulation is that it transforms inhomogeneous boundary conditions into the corresponding homogeneous ones for the primary time-evolving variables, i.e., $\mathbf{u}_v$. A similar approach was used in [19] to deal with inhomogeneous constraints arising in low Mach number combustion, motivated by the corresponding splitting of the velocity field in [13] for the fully compressible case. We have also defined a Bernoulli pressure, π, to absorb all gradients in the split, transformed equations. If the flow is frictionless and purely potential ($\mathbf{u} = \nabla \phi$), the equation of motion (13) reduces to Bernoulli's equation.

The boundary conditions on $\mathbf{u}_v$ are as follows:

(1) along the axis of symmetry

$$\mathbf{u}_v \cdot \mathbf{n} = 0, \tag{15}$$

(2) at the solid wall

$$\mathbf{u}_v \cdot \mathbf{n} = 0$$

$$\mathbf{u}_v \cdot \mathbf{t} = (\mathbf{u}_b - \mathbf{u}_p) \cdot \mathbf{t}, \tag{16}$$

(3) at inflow

$$u_d = 0$$

$$v_d = 1 - 2r^2, \tag{17}$$

(4) at outflow

$$\frac{\partial \mathbf{u}_v}{\partial z} = 0. \tag{18}$$

The boundary condition on p at outflow is $\pi = 0$. It follows that the potential flow solution, $\mathbf{u}_p$ satisfies the Euler equations. These boundary conditions lead to div and grad operators appearing in (13) that are formally adjoints to one another,

$$\int_\Omega \mathrm{div}(\mathbf{w}) \psi \, d\mathcal{V} = -\int_\Omega (\mathbf{w} \cdot \mathrm{grad}(\psi)) \, d\mathcal{V}, \tag{19}$$

if **w** and ψ satisfy the boundary conditions. The reason this is the case is that the boundary conditions for $\mathbf{u}_v$ and π are set so that the boundary terms coming from application of the divergence theorem to $\int_\Omega \nabla \cdot (\mathbf{w}\psi)\, d\mathcal{V}$ vanish. Finally, we can recover equations for **u**:

$$\left.\frac{\partial \mathbf{u}}{\partial t}\right|_\xi = \left.\frac{\partial \mathbf{u}_\mathrm{p}}{\partial t}\right|_\xi + \mathcal{F}(\mathbf{u}_v, \mathbf{u}_\mathrm{p}) - \mathrm{grad}(\pi). \tag{20}$$

3. TIME DISCRETIZATION

Model problem. We use a model problem to address the issue of the time-dependent incompressibility constraint. The model problem is a finite dimensional version of the equation of motion (13). Let $f, u \in \mathcal{R}^n$, $\pi \in \mathcal{R}^m$, and A be an $n \times m$ matrix, where u, A, and f are smooth functions of time. The model system is a differential–algebraic system comprising an equation of motion and a homogeneous, linear constraint:

$$\begin{aligned} \frac{du}{dt} &= f - A^T\pi \\ Au &= 0. \end{aligned} \tag{21}$$

Here u corresponds to the fluid velocity in (13), and f to the advection and viscosity terms. A and A^T are adjoint matrix operators that correspond to div and grad and include boundary conditions.

Integration of systems of differential–algebraic equations has been previously addressed [29]. Methods based on backward differentiation formulae are often used to integrate such systems [26]. In the present work, we use a second-order one-step method, analogous to Heun's method for ODEs, that exploits the special structure of (21).

The constraint can be used to obtain an equation for π. To obtain a "pressure-Poisson" type equation, we differentiate the constraint ($\frac{d}{dt}(Au) = 0$) and compare the result to the divergence of the equation of motion (21), giving

$$L\pi = Af + \frac{dA}{dt}u, \tag{22}$$

where $L \equiv AA^T$. Solvability is assumed for (22). In the case of an incompressible fluid, either L is invertible or it has a null space that is independent of time.

We define operators

$$\begin{aligned} Q &= A^T L^{-1} A \\ P &= I - Q. \end{aligned} \tag{23}$$

In the case where A is independent of time, these operators can be used to eliminate the constraint, yielding

$$\frac{du}{dt} = Pf, \tag{24}$$

with the initial conditions satisfying the constraint $(Au)(0) = 0$. In that case, the BCG discretization reduces to

$$u^{n+1} = u^n + \Delta t P\left(f^{n+\frac{1}{2}}\right) = P\left(u^n + \Delta t f^{n+\frac{1}{2}}\right), \tag{25}$$

where Δt is the discrete time step and $u^0 = u(0)$. This discretization is second-order owing to use of the midpoint rule for f. Also, $P(u^{n+1}) = u^{n+1}$ if $P(u^n) = u^n$.

The BCG discretization can be written in predictor–corrector form as

$$u^* = u^n + \Delta t\left(f^{n+\frac{1}{2}} - A^T\pi^{n-\frac{1}{2}}\right)$$
$$u^{n+1} = P(u^*) \tag{26}$$
$$L\pi^{n+\frac{1}{2}} = \frac{1}{\Delta t}A\left(u^n + \Delta t\left(f^{n+\frac{1}{2}} - A^T\pi^{n-\frac{1}{2}}\right)\right) + L\pi^{n-\frac{1}{2}},$$

where $u^n \approx u(t^n)$ and $\pi^{n-1/2} \approx \pi(t^n - \frac{\Delta t}{2})$.

Next, we generalize the BCG discretization for the model problem with time-dependent A. In the time-independent case, we obtained a second-order accurate method by eliminating the constraint and applying the midpoint rule to the resulting system of ordinary differential equations. A reduction corresponding to (24) does not exist when the constraint is time-dependent, and we must construct a second-order accurate discretization directly for the original constrained system. Such a discretization is given as

$$u^* = u^n + \Delta t\left(f^{n+\frac{1}{2}} - \left(A^{n+\frac{1}{2}}\right)^T\pi^{n-\frac{1}{2}}\right)$$
$$u^{n+1} = P^{n+1}(u^*) = P^{n+1}\left(u^n + \Delta t\left(f^{n+\frac{1}{2}} - \left(A^{n+\frac{1}{2}}\right)^T\pi^{n-\frac{1}{2}}\right)\right) \tag{27}$$
$$L^{n+1}\pi^{n+\frac{1}{2}} = \frac{1}{\Delta t}A^{n+1}\left(u^n + \Delta t\left(f^{n+\frac{1}{2}} - \left(A^{n+\frac{1}{2}}\right)^T\pi^{n-\frac{1}{2}}\right)\right) + L^{n+1}\pi^{n-\frac{1}{2}},$$

where all terms are evaluated at the discrete time, $t = t^{n+1}$, unless otherwise indicated.

Let w^{new} and q^{new} be solutions approximated by the predictor–corrector scheme:

$$w^{\text{new}} = P^{n+1}\left(w + \Delta t\left(f^{n+\frac{1}{2}} + \left(A^{n+\frac{1}{2}}\right)^T q\right)\right)$$
$$q^{\text{new}} = q + \frac{1}{\Delta t}(L^{n+1})^{-1}A^{n+1}\left(w + \Delta t\left(f^{n+\frac{1}{2}} + \left(A^{n+\frac{1}{2}}\right)^T q\right)\right). \tag{28}$$

Define $u_{\text{e}}^n = u(t^n)$ and $\pi_{\text{e}}^{n+1/2} = \pi(t^{n+1/2})$, where u and π are solutions to the model problem (21). If $w = u_{\text{e}}^n$ and $q = \pi_{\text{e}}^{n-1/2} + O(\Delta t)$, then

(1) the method is second-order accurate,

$$w^{\text{new}} = u_{\text{e}}^{n+1} + O(\Delta t^3), \tag{29}$$

and

(2)

$$q^{\text{new}} = \pi_{\text{e}}^{n+\frac{1}{2}} + O(\Delta t). \tag{30}$$

Proof of (1).   To prove the consistency of the predictor–corrector discretization, the solution w^{new} is compared to the standard of a Crank–Nicolson solution which employs the midpoint rule. It is noted that the midpoint rule for ordinary differential equations yields

global second-order accuracy.

$$
\begin{aligned}
w^{\mathrm{mid}} &\equiv u_{\mathrm{e}}^n + \Delta t \left(f^{n+\frac{1}{2}} + (A^T \pi_{\mathrm{e}})^{n+\frac{1}{2}} \right) \\
&= u_{\mathrm{e}}^{n+1} + O(\Delta t^3) \\
P^{n+1} w^{\mathrm{mid}} &= w^{\mathrm{mid}} + O(\Delta t^3) \\
w^{\mathrm{new}} - w^{\mathrm{mid}} &= \Delta t\, P^{n+1} \left(A^{n+\frac{1}{2}} \right)^T \left(\pi_{\mathrm{e}}^{n+\frac{1}{2}} - q \right) + O(\Delta t^3) \\
&= O(\Delta t^3)
\end{aligned}
\tag{31}
$$

since $P^{n+1}(A^{n+1/2})^T$ is $O(\Delta t)$.

Proof of (2).

$$
\begin{aligned}
\pi^{\mathrm{new}} &= q + (L^{n+1})^{-1} \left[\frac{A^{n+1} - A^n}{\Delta t} u_{\mathrm{e}}^n + A^{n+1} f^{n+\frac{1}{2}} + A^{n+1} \left(A^{n+\frac{1}{2}} \right)^T q \right] \\
&= (L^{n+1})^{-1} \left(\frac{A^{n+1} - A^n}{\Delta t} u_{\mathrm{e}}^n + A^{n+1} f^{n+\frac{1}{2}} \right) + A^{n+1} \left(A^{n+\frac{1}{2}} - A^{n+1} \right)^T q \\
&= \pi_{\mathrm{e}}^{n+\frac{1}{2}} + O(\Delta t).
\end{aligned}
\tag{32}
$$

This predictor–corrector discretization requires the application of only a succession of fixed time operators rather than solution of problems resulting from differentiation of the constraint with respect to time. In this fashion, the solution always satisfies the constraint.

4. SPATIAL DISCRETIZATION

In this section, we use the split-velocity formulation and the time-discretization algorithm described in the previous two sections as the basis for developing a numerical method using a time-dependent coordinate transformation to represent the deforming domain. The BCG projection approach has been previously extended to mapped coordinates for the case in which the mapping does not depend on time [9]. However, the extension to moving mapped coordinates has not been done previously.

Discretization of problem domain. To approximate the derivatives, boundary conditions, and the incompressibility constraint in the equations of motion, the spatial and temporal domains are discretized by finite differences. For spatial discretization, a grid is laid out over the spatial domain such that the center of each cell carries the integer indices (i, j). Edges of cells are denoted by $(i + \frac{1}{2}, j)$ and $(i, j + \frac{1}{2})$. The indices of a cell vertex are $(i + \frac{1}{2}, j + \frac{1}{2})$. The discrete difference between two cells is either Δr or Δz, depending on the direction of the gradient.

Time-centering is indicated by a superscript n, corresponding to time $t = t^n$. Given a discrete solution at a time $t = t^n$, the solution is evolved to time $t = t^{n+1}$. The discrete difference in the evolved time is called a time step, $\Delta t = t^{n+1} - t^n$. The object of the numerical algorithm is to successively obtain a solution updated from the previous time increment until the desired final time is reached.

Discrete velocity is a cell-centered quantity and is represented as $U_{i,j}^n$. The vortical component of velocity is also cell-centered, $U_{\mathrm{v},i,j}^n$. The natural centering for the potential
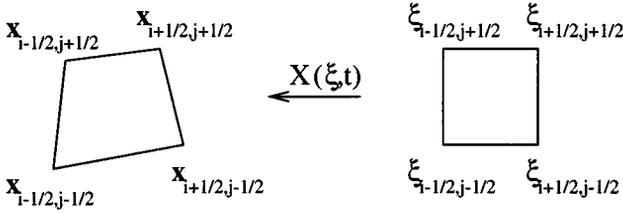
FIG. 2.   Discrete mapping. Time-dependent quadrilateral grid mapped onto a fixed, rectangular grid.

velocity is at edges, $(U^n_{p,i+1/2,j}, U^n_{p,i,j+1/2})$. It can be obtained at cell centers by an averaging process described below. Pressure is a cell-centered term, $\pi^{n+1/2}_{i,j}$, which is centered at the half step in time, $t = t^n + \frac{\Delta t}{2}$. The discrete grid velocity, S, is known at cell vertices and can be averaged to cell edges and centers in the obvious manner.

Discrete mapping.   Our approach to the discretization of this problem uses a moving control-volume discretization of space that has been quite standard in compressible flow calculations for some time. Although we do not discretize the velocity advection terms in conservation form, because of the split-velocity formulation, the spatial discretization used here allows for the addition of conservative transport of other scalars, using the approach in [8].

The transformation of coordinates (2) is used to model irregular domains which result from movement of the solid wall boundary. A mesh composed of quadrilaterals is placed on the real domain of the problem. A logically rectangular, computational space, ξ, is mapped onto the physical space, $\mathbf{x}$ (see Fig. 2). It is in the former space where the time differencing and undivided spatial differencing take place.

Let the edge of each quadrilateral cell represent a tangent vector along a coordinate line (see Fig. 3):

$$
\begin{aligned}
\mathbf{t}^\eta_{i,j+\frac{1}{2}} = \mathbf{x}_{\xi,i,j+\frac{1}{2}} = \mathbf{x}_{i+\frac{1}{2},j+\frac{1}{2}} - \mathbf{x}_{i-\frac{1}{2},j+\frac{1}{2}} \approx \Delta\xi \left.\frac{\partial x}{\partial \xi}\right|_{i,j+\frac{1}{2}} \\
\mathbf{t}^\xi_{i+\frac{1}{2},j} = \mathbf{x}_{\eta_{i\frac{1}{2},j}} = \mathbf{x}_{i+\frac{1}{2},j+\frac{1}{2}} - \mathbf{x}_{i+\frac{1}{2},j-\frac{1}{2}} \approx \Delta\eta \left.\frac{\partial x}{\partial \eta}\right|_{i+\frac{1}{2},j}.
\end{aligned}
\tag{33}
$$

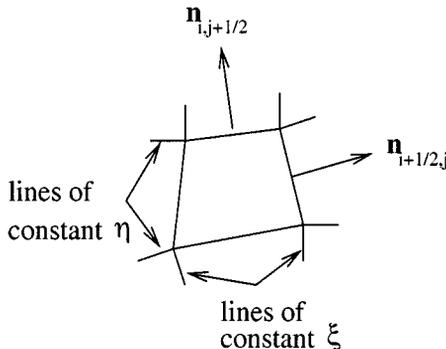Note that the subscripted discretized variables, $\mathbf{x}_{\xi,j+1/2}$, etc., denote undivided differences.

FIG. 3.   Cell volume, edge normals, and indices.

Normal vectors can be defined from the tangents

$$\mathbf{n}^{\eta}_{i,j+\frac{1}{2}} = (-z_\xi, r_\xi)_{i,j+\frac{1}{2}}$$

$$\mathbf{n}^{\xi}_{i+\frac{1}{2},j} = (z_\eta, -r_\eta)_{i+\frac{1}{2},j}$$

(34)

and averaged to cell centers when needed:

$$\mathbf{n}^{\xi}_{i,j} = \frac{1}{2}\left(\mathbf{n}^{\xi}_{i+\frac{1}{2},j} + \mathbf{n}^{\xi}_{i-\frac{1}{2},j}\right)$$

$$\mathbf{n}^{\eta}_{i,j} = \frac{1}{2}\left(\mathbf{n}^{\eta}_{i,j+\frac{1}{2}} + \mathbf{n}^{\eta}_{i,j-\frac{1}{2}}\right).$$

(35)

The volume metrics are similarly defined at cell edges:

$$g^{\eta}_{i,j+\frac{1}{2}} = 2\pi r_{i,j+\frac{1}{2}}$$

$$g^{\xi}_{i+\frac{1}{2},j} = 2\pi r_{i+\frac{1}{2},j}.$$

(36)

These quantities can be averaged to cell centers in the same fashion as for normals. Also, normals can be redefined to include the volume metrics at the respective edges on which they are centered, $\mathbf{n}_g = g\mathbf{n}$.

A discrete definition of the Jacobian of transformation, or cell volume, follows from the tangent equations and is used to calculate the quantity at the half step in time:

$$\sigma^{n+\frac{1}{2}}_{i,j} = g^{n+\frac{1}{2}}_{i,j}\left(\frac{1}{2}\left|\mathbf{t}^{\xi}_{i,j+\frac{1}{2}} \times \mathbf{t}^{\eta}_{i+\frac{1}{2},j}\right| + \frac{1}{2}\left|\mathbf{t}^{\xi}_{i,j-\frac{1}{2}} \times \mathbf{t}^{\eta}_{i-\frac{1}{2},j}\right|\right)^{n+\frac{1}{2}}.$$

(37)

The analytical form of the Jacobian is seen in its representation at a cell edge,

$$\sigma_{i+\frac{1}{2},j} = g^{\eta}_{i+\frac{1}{2},j}\left(r_{\xi_{i+\frac{1}{2},j}}z_{\eta_{i+\frac{1}{2},j}} - r_{\eta_{i+\frac{1}{2},j}}z_{\xi_{i+\frac{1}{2},j}}\right)$$

$$\sigma_{i,j+\frac{1}{2}} = g^{\xi}_{i,j+\frac{1}{2}}\left(r_{\xi_{i,j+\frac{1}{2}}}z_{\eta_{i,j+\frac{1}{2}}} - r_{\eta_{i,j+\frac{1}{2}}}z_{\xi_{i,j+\frac{1}{2}}}\right),$$

(38)

where metrics at other edges are obtained from the four "nearest neighbors":

$$\mathbf{x}_{\xi_{i+\frac{1}{2},j}} = \frac{1}{4}\left(\mathbf{x}_{\xi_{i+1,j+\frac{1}{2}}} + \mathbf{x}_{\xi_{i+1,j-\frac{1}{2}}} + \mathbf{x}_{\xi_{i,j+\frac{1}{2}}} + \mathbf{x}_{\xi_{i,j-\frac{1}{2}}}\right)$$

$$\mathbf{x}_{\eta_{i,j+\frac{1}{2}}} = \frac{1}{4}\left(\mathbf{x}_{\eta_{i+\frac{1}{2},j+1}} + \mathbf{x}_{\eta_{i-\frac{1}{2},j+1}} + \mathbf{x}_{\eta_{i+\frac{1}{2},j}} + \mathbf{x}_{\eta_{i-\frac{1}{2},j}}\right).$$

(39)

The discrete Jacobian is evolved to a new time by conservation of volume [8] using $J_t = \nabla \cdot s$,

$$\sigma^{n+1}_{i,j} = \sigma^{n}_{i,j} + \delta\sigma^{n+\frac{1}{2}}_{i+\frac{1}{2},j} - \delta\sigma^{n+\frac{1}{2}}_{i-\frac{1}{2},j} + \delta\sigma^{n+\frac{1}{2}}_{i,j+\frac{1}{2}} - \delta\sigma^{n+\frac{1}{2}}_{i,j-\frac{1}{2}},$$

(40)

where

$$\delta\sigma^{n+\frac{1}{2}}_{i+\frac{1}{2},j} = g^{n+\frac{1}{2}}_{i+\frac{1}{2},j}\Sigma\left(\mathbf{x}^{n}_{i+\frac{1}{2},j-\frac{1}{2}}, \mathbf{x}^{n}_{i+\frac{1}{2},j+\frac{1}{2}}, \mathbf{x}^{n+1}_{i+\frac{1}{2},j+\frac{1}{2}}, \mathbf{x}^{n+1}_{i+\frac{1}{2},j-\frac{1}{2}}\right)$$

$$\delta\sigma^{n+\frac{1}{2}}_{i,j+\frac{1}{2}} = g^{n+\frac{1}{2}}_{i,j+\frac{1}{2}}\Sigma\left(\mathbf{x}^{n}_{i+\frac{1}{2},j+\frac{1}{2}}, \mathbf{x}^{n}_{i-\frac{1}{2},j+\frac{1}{2}}, x^{n+1}_{i-\frac{1}{2},j+\frac{1}{2}}, \mathbf{x}^{n+1}_{i+\frac{1}{2},j+\frac{1}{2}}\right)$$

(41)

are the partial cell volumes for a moving quadrilateral element (see Fig. 4).
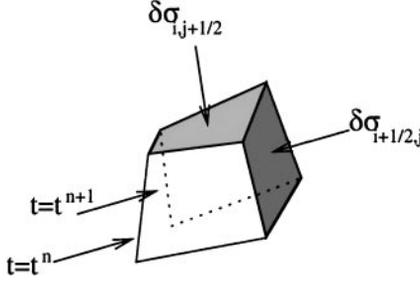
FIG. 4. Representation of the time dependence of J. Cell at t^n moves to t^{n+1} showing partial cell volumes.

Incompressible flow. We now apply the time discretization in the model problem to the split-velocity formulation describing the time evolution of $\mathbf{u}_v$ (13). First, we use the Hodge decomposition to define the semidiscrete version of the operators (23). The Hodge decomposition [11] (derivable from the Helmholtz representation theorem in continuum mechanics [4, 17]) is a splitting of any smooth vector field on a simply connected domain into two orthogonal components: a divergence-free part, $\mathbf{w}_d$, and a gradient of a scalar field, ψ. If $\mathbf{w} = \mathbf{w}(\mathbf{x})$ is a vector field defined on a simply connected domain, Ω, then $\mathbf{w}$ can be orthogonally decomposed as follows:

$$\mathbf{w} = \mathbf{w}_d + \nabla \psi$$
$$\nabla \cdot \mathbf{w}_d = 0, \quad \Delta \psi = \nabla \cdot \mathbf{w}. \tag{42}$$

The boundary condition at ouflow is $\psi = 0$; on the rest of the boundary, $\frac{\partial \psi}{\partial n} = \mathbf{w} \cdot \mathbf{n}$. This decomposition is similar to that performed to obtain the split-velocity form of the equations. However, it differs in that the boundary conditions at outflow are given a condition on the normal component of the velocity, rather than the homogeneous Dirichlet condition on ψ used here.

The projection operators are defined as

$$P(\mathbf{w}) = \mathbf{w}_d$$
$$Q(\mathbf{w}) = \text{grad}(\psi) \tag{43}$$

corresponding to the operators in (23).

Next, we compute a time-centered estimate of the right-hand side corresponding to $f^{n+1/2}$ in the model problem (21). Following [6], we solve the system of equations

$$U^* = U^n + \left(U_p^{n+1} - U_p^n\right)$$
$$+ \Delta t \left[-\mathbf{A}_s(U_v, U_p)^{n+\frac{1}{2}} + \frac{v}{2}\left(\Delta_v^{n+1}(U^*) + \Delta_v^n(U^n)\right) - \nabla^{n+\frac{1}{2}}\pi^{n-\frac{1}{2}}\right], \quad (44)$$

where $U^n = U_v^n + U_p^n$ is the semidiscrete approximation to the solution $\mathbf{u}$. Here, $\mathbf{A}_s(U_v, U_p)^{n+1/2}$ is an estimate of the advective terms at time $t^n + \frac{\Delta t}{2}$, computed using a second-order accurate Godunov method [12]. If $\pi^{n-1/2}$ were replaced by $\pi^{n+1/2}$, this would be a Crank–Nicolson discretization for the diffusion terms. As is, it is suffcient to obtain an $O(\Delta t^2)$ estimate of $\frac{v}{2}(\Delta_v^n(U^n) + \Delta_v^{n+1}(U^*))$.

We apply the discrete evolution by forming

$$U_d^* = U_v^n + \Delta t \left[-\mathbf{A}_s(U_v, U_p)^{n+1/2} + \frac{\nu}{2} \left(\Delta_\nu^{n+1}(U^*) + \Delta_\nu^n(U^n) \right) - \nabla^{n+1/2} \pi^{n-1/2} \right] \quad (45)$$

and obtain the updated solution in pressure correction form:

$$U_v^{n+1} = \mathbf{P}^{n+1}(U_v^*)$$

$$\pi^{n+1/2} = \frac{1}{\Delta t} (\Delta^{n+1})^{-1} (\nabla^{n+1} \cdot U_d^*) + \pi^{n-1/2} \quad (46)$$

$$U_v^{n+1} = U_v^* - \Delta t \nabla^{n+1} (\pi^{n+1/2} - \pi^{n-1/2}).$$

To complete the specification of the algorithm, we must specify the spatial discretization of $\mathbf{P}$, $\Delta \mathbf{u}$, $\mathbf{u} \cdot \nabla \mathbf{u}$, and $\mathbf{u}_p$.

Discrete Hodge projection.   We use an approximate projection of a type first introduced in [1]. The particular discretization we use is a generalization of that in [22], in which the scalar field is cell-centered. First, we define a Laplacian operator based on an edge-centered divergence and gradient:

$$\mathbf{L} = \mathbf{DG}. \quad (47)$$

The divergence operator, $\mathbf{D}$, is discretized based on a finite volume approach to calculation of conservation of mass within a cell (see Fig. 5):

$$(\nabla \cdot U)_{i,j} = \left((g^\xi \mathbf{n}^\xi \cdot U)_{i+1/2,j} - (g^\xi \mathbf{n}^\xi \cdot U)_{i-1/2,j} \right.$$
$$\left. + (g^\eta \mathbf{n}^\eta \cdot U)_{i,j+1/2} - (g^\eta \mathbf{n}^\eta \cdot U)_{i,j-1/2} \right) / \sigma_{i,j}. \quad (48)$$

An undivided difference in the ξ gradient has been dotted into a transformed velocity whose two components are defined at edges which are described by a constant ξ or a constant η line, respectively (denoted by a superscript). The spatial centering of the inverse transformation matrix is seen in this relation where the rows of $\mathbf{F}^{-1}$ are made up of the normals at corresponding edges.
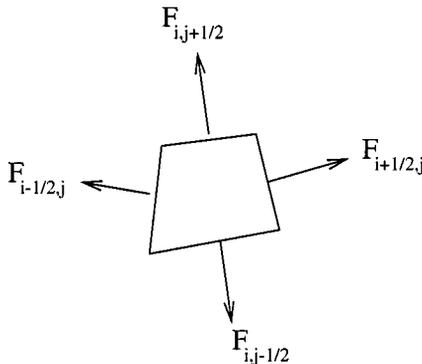

FIG. 5.   Finite volume description of divergence. $F = U \cdot \mathbf{n}_g$ is the flux at an edge of a cell.

The gradient operator, $\mathbf{G}$, is discretized at edges in the following manner:

$$
\begin{aligned}
(\nabla\phi)_{i+\frac{1}{2},j} &= \frac{g^\xi}{\sigma}\begin{bmatrix} z_\eta & -z_\xi \\ -r_\eta & r_\xi \end{bmatrix}_{i+\frac{1}{2},j}\begin{bmatrix} \phi_{i+1,j}-\phi_{i,j} \\ \frac{1}{4}(\phi_{i+1,j+1}+\phi_{i,j+1}-\phi_{i+1,j-1}-\phi_{i,j-1}) \end{bmatrix} \\
(\nabla\phi)_{i,j+\frac{1}{2}} &= \frac{g^\eta}{\sigma}\begin{bmatrix} z_\eta & -z_\xi \\ -r_\eta & r_\xi \end{bmatrix}_{i,j+\frac{1}{2}}\begin{bmatrix} \frac{1}{4}(\phi_{i+1,j+1}+\phi_{i+1,j}-\phi_{i-1,j+1}-\phi_{i-1,j}) \\ \phi_{i+1j}-\phi_{i,j} \end{bmatrix}.
\end{aligned}
\tag{49}
$$

Boundary conditions are applied to $\mathbf{L}$ when the stencil for the gradient extends beyond the problem domain. At edges orthogonal to boundaries, ϕ is extrapolated into a "ghost" cell to calculate the transverse component of $\nabla_\xi\phi$. For example, at the $i=\frac{1}{2}$ edge,

$$
\phi_{0,j} = 3(\phi_{1,j}-\phi_{2,j})+\phi_{3,j},
\tag{50}
$$

where the subscript 0 denotes the ghost cell value.

The cell-centered divergence operator, $\mathbf{D}_0$, is actually an edge-centered divergence operator applied to edge-centered velocities which have been averaged from cell centers, $\mathbf{w}_{i+1/2,j} = \frac{\mathbf{w}_{i+1,j}+\mathbf{w}_{i,j}}{2}$, for example. The boundary conditions are those given in (15)–(18), where the outflow condition is discretized using an extrapolation from the interior:

$$
(U\cdot\mathbf{n})_{i,Nz+\frac{1}{2}} = \left(\frac{3}{2}U_{i,N_z-\frac{1}{2}}-\frac{1}{2}U_{i,N_z-\frac{3}{2}}\right)\cdot\mathbf{n}.
\tag{51}
$$

The cell-centered gradient operator, $\mathbf{G}_0$, is a more complicated discretization. The procedure for computing $\mathbf{G}_0\phi_{i,j}$ is

(1) Compute the edge-centered gradients, $(\mathbf{G}\phi)_{i+1/2,j}$ and $(\mathbf{G}\phi)_{i,j+1/2}$, on interior edges.
(2) Linearly extrapolate the vectors $(\mathbf{G}\phi)_{i+1/2,j}$, $(\mathbf{G}\phi)_{i,j+1/2}$ to boundaries.
(3) Compute $\mathbf{n}\cdot\mathbf{G}\phi$ at all edges.
(4) Compute $(\mathbf{G}_0\phi)_{i,j}$ by solving the equations

$$
\begin{aligned}
\mathbf{n}^\xi_{i,j}\cdot(\mathbf{G}_0\phi)_{i,j} &= \left[(\mathbf{n}\cdot\mathbf{G}\phi)_{i+\frac{1}{2},j}+(\mathbf{n}\cdot\mathbf{G}\phi)_{i-\frac{1}{2},j}\right]/2 = a^\xi_{i,j} \\
\mathbf{n}^\eta_{i,j}\cdot(\mathbf{G}_0\phi)_{i,j} &= \left[(\mathbf{n}\cdot\mathbf{G}\phi)_{i,j+\frac{1}{2}}+(\mathbf{n}\cdot\mathbf{G}\phi)_{i,j-\frac{1}{2}}\right]/2 = a^\eta_{i,j}
\end{aligned}
\tag{52}
$$

$$
\Rightarrow (\mathbf{G}_0\phi)_{i,j} = \frac{1}{(r_\xi z_\eta - r_\eta z_\xi)_{i,j}}\begin{bmatrix} r_\xi & r_\eta \\ z_\xi & z_\eta \end{bmatrix}_{i,j}\begin{bmatrix} a^\xi \\ a^\eta \end{bmatrix}_{i,j},
$$

where the normal, $\mathbf{n}$, without the volume metric is used in the calculation of the cell-centered pressure gradient for consistency.

Boundary conditions for edge-centered gradients in the cell-centered calculation are a linear extrapolation of $\mathbf{G}\phi$ from interior edges,

$$
(\mathbf{G}\phi)_{\frac{1}{2},j} = 2(\mathbf{G}\phi)_{\frac{3}{2},j}-(\mathbf{G}\phi)_{\frac{5}{2},j},
\tag{53}
$$

for example, at the axis of symmetry boundary edge, $i=\frac{1}{2}$.

We now define the approximate projection operator appearing in (46) as

$$
\mathbf{P} = (\mathbf{I}-\mathbf{G}_0\mathbf{L}^{-1}\mathbf{D}_0).
\tag{54}
$$

FIG. 6. Discrete representation of solution to an elliptic equation.

We demonstrate how the solution procedure described above gives the solution to the inhomogeneous problem. $\mathbf{D}_0$ and $\mathbf{L}$ have homogeneous boundary conditions. However, we are solving an inhomogeneous problem (42). Consider the following elliptic equation and its graphic representation in Fig. 6:

$$\mathbf{L}\phi = \nabla \cdot \mathcal{F}. \tag{55}$$

In general, the potential, ϕ, is composed of a homogeneous part, ϕ_H, and an inhomogeneous part, ϕ_B:

$$\phi = \phi_H + \phi_B. \tag{56}$$

ϕ_H is the solution to the homogeneous problem,

$$\mathbf{L}_H \phi_H = \mathbf{D}\mathcal{F}, \tag{57}$$

with $\mathbf{n} \cdot \mathbf{G}\phi_H = 0$ on the boundary. The boundary conditions for $\mathbf{L}_H$ are homogeneous and extrapolated for the flux of $\mathcal{F}$ in the divergence. The other part, ϕ_B, satisfies the inhomogeneous problem

$$\mathbf{L}_I \phi_B = 0 \tag{58}$$

with $\mathbf{n} \cdot \mathbf{G}\phi_B = \mathcal{H}$ on the boundary, where $\mathcal{H} = \mathbf{n} \cdot \mathcal{F}$ is an inhomogeneous boundary condition which contains the normal component of the extrapolated piece of $\mathcal{F}$ from the divergence flux at the boundary in the homogeneous step. The inhomogeneous problem is rewritten into an equivalent one for the homogeneous operator by transferring the inhomogeneity in $\mathbf{L}_I$ to the right-hand side of the equation (see Fig. 6), giving

$$\mathbf{L}_H \phi_B = \mathbf{D}(-\mathcal{H}) \tag{59}$$

with $\mathbf{n} \cdot \mathbf{G}\phi_B = 0$ on the boundary. The homogeneous problem and the equivalent inhomogeneous problem can now be added into one discrete equation since the same operator, $\mathbf{L}_H$, is used in both:

$$\mathbf{L}_H \phi = \mathbf{D}(\mathcal{F} - \mathcal{H}). \tag{60}$$

A key observation in the numerical implementation of the projection is that the extrapolated boundary condition for the divergence of $\mathcal{F}$ is consumed in the pressure and is never seen in the actual discretization. Also, desirable homogeneous boundary conditions are applied to fluxes of $\mathcal{F}$ in the divergence at boundaries since the pressure is carrying the extrapolated piece.

Discrete Laplacian operator. The Laplacian operator is based upon a nine-point stencil for quadrilateral grids. The stencil is the same throughout the algorithm with the only variation being boundary conditions on $\nabla\phi$. The Laplacian of ϕ at cell (i, j) can be expressed as a weighted sum of the values of ϕ at (i, j) and at its nearest neighbors:

$$(\mathbf{L}\phi)_{i,j} = \frac{1}{\sigma_{i,j}} \Sigma a_{\vec{s}} \phi_{\vec{i}+\vec{s}}. \tag{61}$$

The stencil coefficients, $a_{\vec{s}}$, are defined as

$$a_{-1,1} = \left((G^\xi s)_{i-\frac{1}{2},j} + (G^\eta s)_{i,j+\frac{1}{2}}\right)/4$$
$$a_{0,1} = \left(-(G^\xi s)_{i+\frac{1}{2},j} + (G^\xi s)_{i-\frac{1}{2},j}\right)/4 + (G^\eta l^\xi)_{i,j+\frac{1}{2}}$$
$$a_{1,1} = \left(-(G^\xi s)_{i+\frac{1}{2},j} - (G^\eta s)_{i,j+\frac{1}{2}}\right)/4$$
$$a_{-1,0} = \left((G^\eta s)_{i,j+\frac{1}{2}} - (G^\eta s)_{i,j-\frac{1}{2}}\right)/4 + (G^\xi l^\eta)_{i-\frac{1}{2},j}$$
$$a_{0,0} = -(G^\xi l^\eta)_{i-\frac{1}{2},j} - (G^\xi l^\eta)_{i+\frac{1}{2},j} - (G^\eta l^\xi)_{i,j+\frac{1}{2}} - (G^\eta l^\xi)_{i,j-\frac{1}{2}} \tag{62}$$
$$a_{1,0} = \left(-(G^\eta s)_{i,j+\frac{1}{2}} + (G^\eta s)_{i,j-\frac{1}{2}}\right)/4 + (G^\xi l^\eta)_{i+\frac{1}{2},j}$$
$$a_{-1,-1} = \left(-(G^\xi s)_{i-\frac{1}{2},j} - (G^\eta s)_{i,j-\frac{1}{2}}\right)/4$$
$$a_{0,-1} = \left((G^\xi s)_{i+\frac{1}{2},j} - (G^\xi s)_{i-\frac{1}{2},j}\right)/4 + (G^\eta l^\xi)_{i,j-\frac{1}{2}}$$
$$a_{1,-1} = \left((G^\xi s)_{i+\frac{1}{2},j} + (G^\eta s)_{i,j-\frac{1}{2}}\right)/4,$$

where

$$G^\xi \equiv \frac{g^\xi}{r_\xi z_\eta - r_\eta z_\xi}$$
$$G^\eta \equiv \frac{g^\eta}{r_\xi z_\eta - r_\eta z_\xi}$$
$$l^\xi \equiv r_\xi^2 + z_\xi^2 \tag{63}$$
$$l^\eta \equiv r_\eta^2 + z_\eta^2$$
$$s \equiv r_\xi r_\eta + z_\xi z_\eta.$$

Viscous operator. The viscous operator, $\mathbf{L}_\nu$, possesses the same stencil as the discrete Laplacian operator, $\mathbf{L}$, on the interior, but differs at the boundaries where physical boundary conditions are applied. The boundary conditions are

(1) along the axis of symmetry

$$u^* = 0$$
$$\frac{\partial v^*}{\partial z} = 0,$$

(64)

(2) at the solid wall (prescribed wall velocity)

$$U^* = U_b^{n+1},$$

(65)

(3) at inflow (Poiseuille flow)

$$u^* = 0$$
$$v^* = 2(1 - r^2),$$

(66)

(4) at outflow

$$\frac{\partial U^*}{\partial z} = 0.$$

(67)

Inhomogeneous boundary conditions, $U^* = U_b$, are applied using a higher order extrapolation in the following manner:

$$U^* = a\xi^2 + b\xi + c$$
$$\left.\frac{\partial U^*}{\partial \xi}\right|_{\text{wall}} = b = -3U_{N_r}^* + \frac{1}{3}U_{N_r-1}^* + \frac{8}{3}U_b^{n+1}$$
$$\left.\frac{\partial U^*}{\partial \eta}\right|_{\text{wall}} = \frac{\partial U_b^{n+1}}{\partial \eta}.$$

(68)

Potential flow solution. The potential velocity, $U_p = \nabla\phi$, can be obtained at any time, t^n, given the special boundary conditions for U^n at inflow and outflow and the prescribed velocity of the solid wall. The solution is obtained by solving Laplace's equation,

$$\mathbf{L}^n\phi = 0,$$

(69)

where the boundary conditions for the solution are given in (8)–(11).

Once the solution to (69) is found, the edge-centered gradient is applied to the potential to obtain the edge-centered potential velocity:

$$U_p^n = \mathbf{G}^n\phi.$$

(70)

These velocities can be averaged to cell centers using the averaging procedure described above for $\mathbf{G}_0$.

Convective discretization. The nonlinear convective derivative, $\mathbf{A}_s(U_v, U_p)^{n+1/2}$, in (14) is calculated using a second-order Godunov method with a projection to account for the pressure [6, 22]. First, the cell-centered velocity, $U_{v,i,j}^n$, is extrapolated to cell edges and to the half step in time by Taylor series expansion, where the effect of pressure is omitted. An edge-centered projection similar to that used in [7, 18] is then applied to enforce the incompressibility constraint on $U_v^{n+1/2}$. Nonconservative differencing is used to
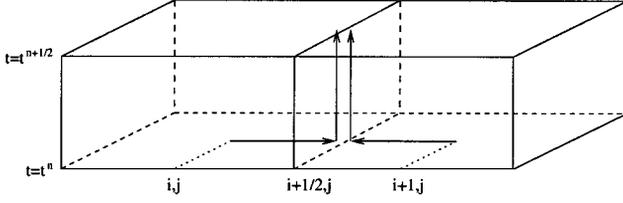
FIG. 7. Godunov box depicting extrapolation of cell-centered velocities to edges and to the half step in time.

approximate $\mathbf{A}_s(U_v, U_p)^{n+1/2}$. There is a time step restriction for the entire algorithm because of the explicit convective discretization.

The discrete divergence-free velocity, $U_{v,i,j}^n$, is expanded to the half step in time, $t^n + \frac{\Delta t}{2}$, and to cell edges in a Taylor series (see Fig. 7):

$$\hat{U}_{v,i+\frac{1}{2},j}^{n+\frac{1}{2}} = U_{v,i,j}^n + \frac{\Delta\xi}{2}\frac{\partial U_v^{n+\frac{1}{2}}}{\partial\xi} + \frac{\Delta t}{2}\frac{\partial U_v}{\partial t}\bigg|_\xi^{n+\frac{1}{2}}. \tag{71}$$

The term $\frac{\partial U_v}{\partial t}|_\xi$ (without the pressure gradient) is then substituted from (13) into (71). The velocities at constant ξ edges are extrapolated from cell-centered values to the left (denoted by L) and to the right (R) of an edge:

$$\hat{U}_{v,i+\frac{1}{2},j}^{n+\frac{1}{2},L} = U_{i,j}^n + \frac{1}{2}\left(1 - \bar{u}_{s,i,j}^{\text{upw},n}\frac{\Delta t}{\sigma_{i,j}^n}\right)\frac{\partial U_v^n}{\partial\xi_{i,j}} - \frac{\Delta t}{2}\left(\frac{\bar{v}_{i,j}^n}{\sigma_{i,j}^n}\right)\left[\frac{\partial U_v}{\partial\eta}\right]_{i,j}^n$$
$$- \frac{\Delta t}{2}\left(\bar{u}_{v,i,j}^n\frac{\partial U_p^n}{\partial\xi_{i,j}} + \bar{v}_{v,i,j}^n\frac{\partial U_p^n}{\partial\eta_{i,j}}\right) - \frac{\nu\Delta t}{2}\mathbf{L}_v^n U_{i,j}^n$$
$$\hat{U}_{v,i+\frac{1}{2},j}^{n+\frac{1}{2},R} = U_{i+1,j}^n - \frac{1}{2}\left(1 + \bar{u}_{s,i+1,j}^{\text{upw},n}\frac{\Delta t}{\sigma_{i+1,j}^n}\right)\frac{\partial U_v^n}{\partial\xi_{i+1,j}} + \frac{\Delta t}{2}\left(\frac{\bar{v}_{i+1,j}^n}{\sigma_{i+1,j}^n}\right)\left[\frac{\partial U_v}{\partial\eta}\right]_{i+1,j}^n$$
$$+ \frac{\Delta t}{2}\left(\bar{u}_{v,i,j}^n\frac{\partial U_p^n}{\partial\xi_{i,j}} + \bar{v}_{v,i,j}^n\frac{\partial U_p^n}{\partial\eta_{i,j}}\right) + \frac{\nu\Delta t}{2}\mathbf{L}_v^n U_{i,j}^n. \tag{72}$$

Velocities are computed in a similar manner at constant η edges where the directions L and R are referred to the subscript j:

$$\hat{U}_{v,i,j+\frac{1}{2}}^{n+\frac{1}{2},L} = U_{i,j}^n + \frac{1}{2}\left(1 - \bar{v}_{i,j}^{\text{upw},n}\frac{\Delta t}{\sigma_{i,j}^n}\right)\frac{\partial U_v^n}{\partial\eta_{i,j}} - \frac{\Delta t}{2}\left(\frac{\bar{u}_{s,i,j}^n}{\sigma_{i,j}^n}\right)\left[\frac{\partial U_v}{\partial\xi}\right]_{i,j}^n$$
$$- \frac{\Delta t}{2}\left(\bar{u}_{v,i,j}^n\frac{\partial U_p^n}{\partial\xi_{i,j}} + \bar{v}_{v,i,j}^n\frac{\partial U_p^n}{\partial\eta_{i,j}}\right) - \frac{\nu\Delta t}{2}\mathbf{L}_v^n U_{i,j}^n$$
$$\hat{U}_{v,i,j+\frac{1}{2}}^{n+\frac{1}{2},R} = U_{i,j+1}^n - \frac{1}{2}\left(1 + \bar{v}_{i,j+1}^{\text{upw},n}\frac{\Delta t}{\sigma_{i,j+1}^n}\right)\frac{\partial U_v^n}{\partial\eta_{i,j+1}} + \frac{\Delta t}{2}\left(\frac{\bar{u}_{s,i,j+1}^n}{\sigma_{i,j+1}^n}\right)\left[\frac{\partial U_v}{\partial\xi}\right]_{i,j+1}^n$$
$$+ \frac{\Delta t}{2}\left(\bar{u}_{v,i,j}^n\frac{\partial U_p^n}{\partial\xi_{i,j}} + \bar{v}_{v,i,j}^n\frac{\partial U_p^n}{\partial\eta_{i,j}}\right) + \frac{\nu\Delta t}{2}\mathbf{L}_v^n U_{i,j}^n. \tag{73}$$

A transformed "upwind" velocity is used for the convective velocity,

$$\bar{u}_s^{\text{upw}} = \max(\bar{u} - \bar{s}, 0)$$
$$\bar{v}^{\text{upw}} = \max(\bar{v}, 0), \tag{74}$$

where the transformed velocity, $\bar{U} = J\,\mathbf{F}^{-1}U$, is centered component wise,

$$\bar{u}_{i,j} = g_{i,j}(z_{\eta i,j}u_{i,j} - r_{\eta i,j}v_{i,j})$$
$$\bar{v}_{i,j} = g_{i,j}(-z_{\xi i,j}u_{i,j} + r_{\xi i,j}v_{i,j}). \tag{75}$$

The slopes in the normal direction of the spatial expansion in the Taylor extrapolation are approximated by centered undivided differences with one-sided differences at the boundary:

$$\frac{\partial U_v^n}{\partial \xi_{i,j}} \approx \frac{U_{v,i+1,j} - U_{v,i-1,j}}{2}$$
$$\frac{\partial U_v^n}{\partial \eta_{i,j}} \approx \frac{U_{v,i,j+1} - U_{v,i,j-1}}{2}. \tag{76}$$

The slopes in the tranverse direction are given by

$$\left[\frac{\partial U_v}{\partial \xi}\right]_{i,j}^n \approx \begin{cases} \hat{U}_{v,i,j}^n - \hat{U}_{v,i-1,j}^n & \text{if } (\bar{u}_{i,j}^n - \bar{s}_{i,j}^n) \geq 0 \\ \hat{U}_{v,i+1,j}^n - \hat{U}_{v,i,j}^n & \text{if } (\bar{u}_{i,j}^n - \bar{s}_{i,j}^n) < 0 \end{cases}$$
$$\left[\frac{\partial U_v}{\partial \eta}\right]_{i,j}^n \approx \begin{cases} \hat{U}_{v,i,j}^n - \hat{U}_{v,i,j-1}^n & \text{if } \bar{v}_{i,j}^n \geq 0 \\ \hat{U}_{v,i,j+1}^n - \hat{U}_{v,i,j}^n & \text{if } \bar{v}_{i,j}^n < 0, \end{cases} \tag{77}$$

with an instability correction for the diffusive, viscous term pointed out by Minion [25]:

$$\hat{U}_{v,i,j}^n = U_{v,i,j}^n + \frac{\nu \Delta t}{2}\Delta U_{i,j}^n. \tag{78}$$

The slopes of the potential velocity are calculated from the edge-centered quantities

$$\frac{\partial U_p^n}{\partial \xi_{i,j}} \approx U_{p,i+\frac{1}{2},j} - U_{p,i-\frac{1}{2},j}$$
$$\frac{\partial U_p^n}{\partial \eta_{i,j}} \approx U_{p,i,j+\frac{1}{2}} - U_{p,i,j-\frac{1}{2}}. \tag{79}$$

At each cell edge, a Riemann problem exists where there is a left and right state from which to choose based on the upwind, convective velocity,

$$\hat{U}_{v,i+\frac{1}{2},j}^{n+\frac{1}{2}} = \begin{cases} U_v^L & \text{if } \bar{u}_s^{\text{upw,l}}, \bar{u}_s^{\text{upw,r}} > 0 \\ U_v^R & \text{if } \bar{u}_s^{\text{upw,l}}, \bar{u}_s^{\text{upw,r}} < 0 \\ \frac{U_v^L + U_v^R}{z} & \text{if } \bar{u}_s^{\text{upw,l}}\bar{u}_s^{\text{upw,r}} \leq 0 \end{cases} \tag{80}$$

$$\hat{U}_{v,i,j+\frac{1}{2}}^{n+\frac{1}{2}} = \begin{cases} U_v^L & \text{if } \bar{v}^{\text{upw,l}}, \bar{v}^{\text{upw,r}} > 0 \\ U_v^R & \text{if } \bar{v}^{\text{upw,l}}, \bar{v}^{\text{upw,r}} < 0 \\ \frac{U_v^L + U_v^R}{z} & \text{if } \bar{v}^{\text{upw,l}}\bar{v}^{\text{upw,r}} \leq 0, \end{cases} \tag{81}$$

where these upwind, convective velocities are defined as

$$
\begin{aligned}
\bar{u}_s^{\text{upw,l}} &\equiv \left(U_{i,j}^n - S_{i+\frac{1}{2},j}^{n+\frac{1}{2}} \right) \cdot \mathbf{n}_{i+\frac{1}{2},j}^{\xi n+\frac{1}{2}} \\
\bar{u}_s^{\text{upw,r}} &\equiv \left(U_{i+1,j}^n - S_{i+\frac{1}{2},j}^{n+\frac{1}{2}} \right) \cdot \mathbf{n}_{i+\frac{1}{2},j}^{\xi n+\frac{1}{2}} \\
\bar{v}^{\text{upw,l}} &\equiv \left(U_{i,j}^n - S_{i,j+\frac{1}{2}}^{n+\frac{1}{2}} \right) \cdot \mathbf{n}_{i,j+\frac{1}{2}}^{\eta n+\frac{1}{2}} \\
\bar{v}^{\text{upw,r}} &\equiv \left(U_{i,j+1}^n - S_{i,j+\frac{1}{2}}^{n+\frac{1}{2}} \right) \cdot \mathbf{n}_{i,j+\frac{1}{2}}^{\eta n+\frac{1}{2}}.
\end{aligned}
\tag{82}
$$

The boundary conditions for the upwind, extrapolated edge-centered velocities are the prescribed conditions (15)–(18) for U_v. At boundaries where the condition is of Neumann form, the extrapolated left or right state—whichever is on the interior side of the boundary edge—is used.

The edge-centered velocities are projected to account for the effect of the pressure gradient at $t^{n+1/2}$ which was omitted in the Taylor extrapolation,

$$
\mathbf{L}\phi_{i,j}^{n+\frac{1}{2}} = \mathbf{D}\hat{U}^{n+\frac{1}{2}},
\tag{83}
$$

where these operators are defined in the discussion of the discrete Hodge projection. The velocities are corrected by edge-centered gradients accordingly:

$$
\begin{aligned}
U_{v,i+\frac{1}{2},j}^{n+\frac{1}{2}} &= \hat{U}_{v,i+\frac{1}{2},j}^{n+\frac{1}{2}} - \nabla\phi_{i+\frac{1}{2},j}^{n+\frac{1}{2}} \\
U_{v,i,j+\frac{1}{2}}^{n+\frac{1}{2}} &= \hat{U}_{v,i,j+\frac{1}{2}}^{n+\frac{1}{2}} - \nabla\phi_{i,j+\frac{1}{2}}^{n+\frac{1}{2}}.
\end{aligned}
\tag{84}
$$

Boundary conditions for the gradients are homogeneous Neumann, $\frac{\partial\phi}{\partial n} = 0$, at all boundaries except outflow, where the boundary condition is homogeneous Dirichlet, $\phi = 0$. This is discretized by setting the ghost cell value $\phi_0 = -\phi_1$.

The nonlinear convective derivative, $\mathbf{A}_s = (U - S) \cdot \nabla U_v + U_v \cdot \nabla U_p$, is calculated using nonconservative differencing with the formula

$$
((U - S) \cdot \nabla U_v)_{i,j}^{n+\frac{1}{2}} = \frac{1}{\sigma_{i,j}^{n+\frac{1}{2}}} \left(\bar{u}_{s,i,j}^{n+\frac{1}{2}} \frac{\partial U_v}{\partial \xi} + \bar{v}_{i,j}^{n+\frac{1}{2}} \frac{\partial U_v}{\partial \eta} \right),
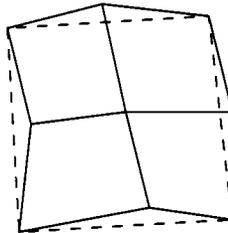\tag{85}
$$

FIG. 8. Grid coarsening. Solid lines indicate fine grid cells and dotted lines indicate coarse grid cell.
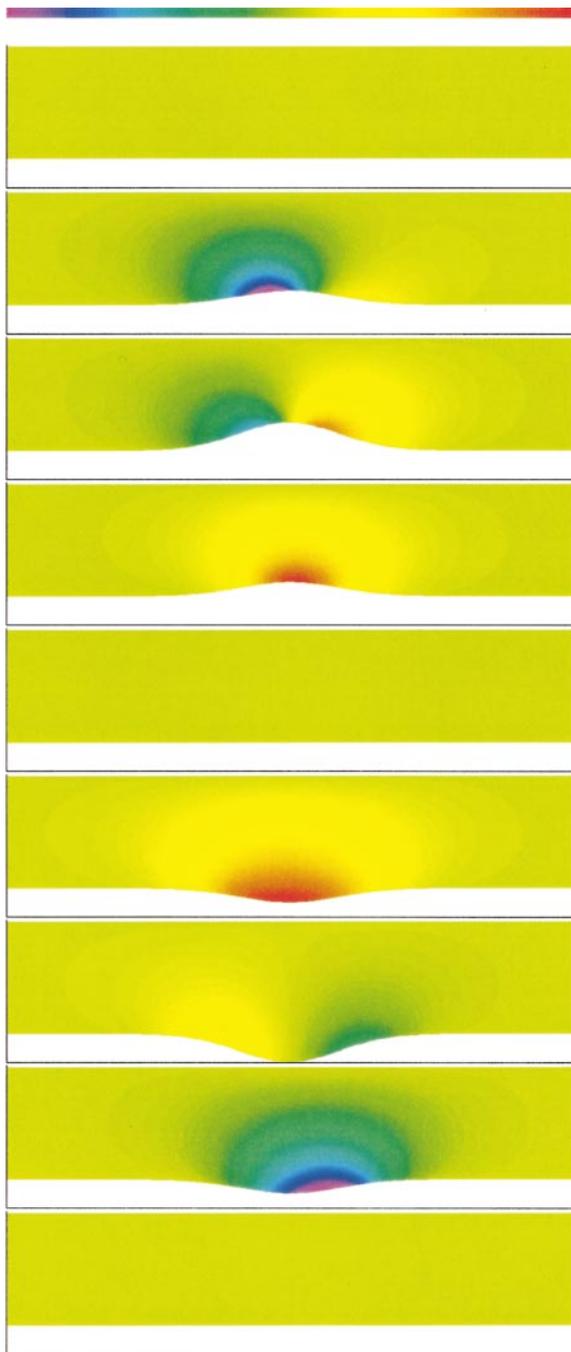
FIG. 9. Radial potential velocity, u_p, at times $t = 0, 0.5, 1, 1.5, 2, 2.5, 3, 3.5, 4$. (Scale: -0.945 to 0.780).
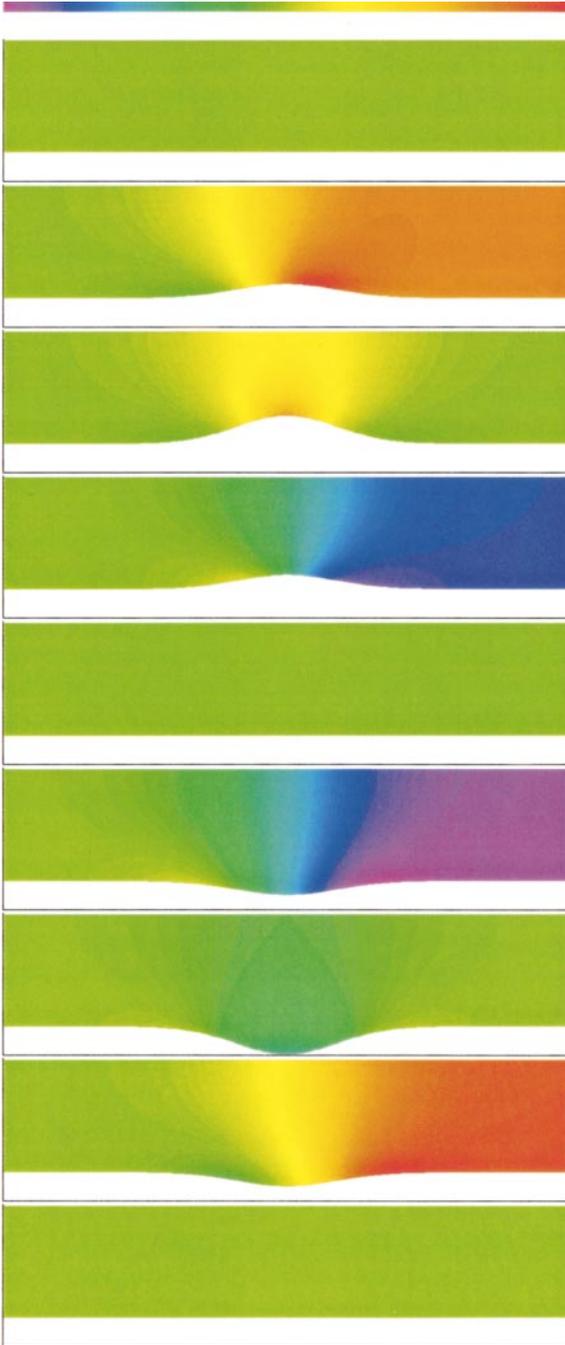
FIG. 10.   Axial potential velocity, v_p, at times $t = 0, 0.5, 1, 1.5, 2, 2.5, 3, 3.5, 4$. (Scale: -0.638 to 2.748).

where

$$\bar{u}_{s,i,j}^{n+\frac{1}{2}} = \frac{1}{2}\left(\bar{u}_{s,i+\frac{1}{2},j}^{n+\frac{1}{2}} + \bar{u}_{s,i-\frac{1}{2},j}^{n+\frac{1}{2}}\right)$$

$$\bar{v}_{i,j}^{n+\frac{1}{2}} = \frac{1}{2}\left(\bar{v}_{i,j+\frac{1}{2}}^{n+\frac{1}{2}} + \bar{v}_{i,j-\frac{1}{2}}^{n+\frac{1}{2}}\right)$$

$$\frac{\partial U_{\mathrm{v}}}{\partial \xi} = U_{\mathrm{v},i+\frac{1}{2},j}^{n+\frac{1}{2}} - U_{\mathrm{v},i-\frac{1}{2},j}^{n+\frac{1}{2}}$$

$$\frac{\partial U_{\mathrm{v}}}{\partial \eta} = U_{\mathrm{v},i,j+\frac{1}{2}}^{n+\frac{1}{2}} - U_{\mathrm{v},i,j-\frac{1}{2}}^{n+\frac{1}{2}}.$$

(86)

The solid wall boundary condition is $\bar{u}_s^{n+1/2}|_{\mathrm{wall}} = 0$ because $U \cdot \mathbf{n}|_{\mathrm{wall}} = S \cdot \mathbf{n}|_{\mathrm{wall}}$.

The part of $\mathbf{A}_s$ due to the potential velocity is similarly calculated via

$$(U_{\mathrm{v}} \cdot \nabla U_{\mathrm{p}})_{i,j}^{n+\frac{1}{2}} = \frac{1}{\sigma_{i,j}^{n+\frac{1}{2}}}\left(\bar{u}_{\mathrm{v},i,j}^{n+\frac{1}{2}}\frac{\partial U_{\mathrm{p}}}{\partial \xi} + \bar{v}_{\mathrm{v},i,j}^{n+\frac{1}{2}}\frac{\partial U_{\mathrm{p}}}{\partial \eta}\right),$$

(87)

where

$$\bar{u}_{\mathrm{v},i,j}^{n+\frac{1}{2}} = \frac{1}{2}\left(\bar{u}_{\mathrm{v},i+\frac{1}{2},j}^{n+\frac{1}{2}} + \bar{u}_{\mathrm{v},i-\frac{1}{2},j}^{n+\frac{1}{2}}\right)$$

$$\bar{v}_{\mathrm{v},i,j}^{n+\frac{1}{2}} = \frac{1}{2}\left(\bar{v}_{\mathrm{v},i,j+\frac{1}{2}}^{n+\frac{1}{2}} + \bar{v}_{\mathrm{v},i,j-\frac{1}{2}}^{n+\frac{1}{2}}\right)$$

$$\frac{\partial U_{\mathrm{p}}}{\partial \xi} = U_{\mathrm{p},i+\frac{1}{2},j}^{n+\frac{1}{2}} - U_{\mathrm{p},i-\frac{1}{2},j}^{n+\frac{1}{2}}$$

$$\frac{\partial U_{\mathrm{p}}}{\partial \eta} = U_{\mathrm{p},i,j+\frac{1}{2}}^{n+\frac{1}{2}} - U_{\mathrm{p},i,j-\frac{1}{2}}^{n+\frac{1}{2}}.$$

(88)

The second-order Godunov method is an explicit scheme. The time step of the entire algorithm is restricted by the Courant–Friedrichs–Lewy (CFL) condition for stability:

$$\Delta t = 0.9/\max_{i,j}\left(\frac{|\bar{u}_{i,j} - \bar{s}_{i,j}|}{\sigma_{i,j}}, \frac{|\bar{v}_{i,j}|}{\sigma_{i,j}}\right).$$

(89)

Solvers.   Each time step of the method requires solution of five elliptic equations: two potential flow solutions, one at time $t^{n+1/2}$ and the other at time t^{n+1}; an edge-centered projection at time $t^{n+1/2}$; solution of the heat equation for the viscous terms; and an approximate projection at time t^{n+1}. We use the multigrid method to solve the linear systems arising from the discretization of the elliptic and parabolic equations given here. This is not an essential feature of the algorithm; any of a variety of modern iterative methods, such as those described in [5], would have been appropriate.

5. RESULTS

We present results for incompressible, viscous flow in an axisymmetric deforming tube. The flow is characterized by Reynolds number, $\mathrm{Re} = \frac{\bar{v}d}{\nu}$, where $\bar{v}$ is the mean velocity, d is the diameter of the tube ($d = 2$ in all cases), and ν is the kinematic viscosity. The grid motion used (see Fig. 1 for geometry) is

$$R(t) = R_0\left\{1 - \frac{1}{4}[1 - \sin\pi(.5 + t)]\right\}\exp[-4(z - z_c)^2],$$

(90)

TABLE I
Error for Flow in Deforming Tube (Re = 8)

Case	$e^{1/16}$	Rate	$e^{1/32}$	Rate	$e^{1/64}$
u	4.01e-3	1.69	1.24e-3	1.75	3.68e-4
v	8.25e-3	2.04	2.01e-3	2.01	4.99e-4

where R_0 is a radius of unity for an initially rectangular grid and z_c is the axial location of the extremum for a Gaussian movement. The tube wall is initially fixed and flat. It moves inward to a fully pinched position ($t = 1$) and back out through the flat position ($t = 2$) to a fully bulged position ($t = 3$) and flat again ($t = 4$). Maximum wall speeds occur at the halfway points between the flat position and the hump maxima. All color figures have been generated by the visualization graphics package described in [16].

We present the convergence results of two flow regimes. The first case is a low Reynolds number calculation, Re = 8, where $\bar{v} = 1$ and $v = 0.25$. The convergence results for this case are shown in Table I at a time when the inward boundary velocity is at a maximum. The second case is a higher Reynolds number calculation, Re = 200, where $\bar{v} = 1$ and $v = 0.01$. The convergence results for this case are shown in Table II at a time when the boundary has stopped moving. The error in the solution is estimated using the standard Richardson procedure. We compute the solution on a series of grids, each of which is refined by a factor of 2 in each coordinate direction over the next coarser one (see Fig. 8). The estimate of the error is computed by averaging the result on a given grid onto the next coarser one and subtracting the two results. Since we expect the solution to be no more than second order, ordinary arithmetic averaging of the cell-centered data is used:

$$\text{Average}(q)_{i,j} = \frac{(q_{2i,2j} + q_{2i+1,2j} + q_{2i,2j+1} + q_{2i+1,2j+1})}{4}.$$

First, we present results for potential flow. Figure 9 shows the radial component of the potential velocity. We note that u_p in general follows the boundary movement. Figure 10 shows the axial component. Conservation of mass is demonstrated: v_p equals the plug flow velocity when the boundary is flat and not moving; v_p increases at the outflow as the result of the pinching of the boundary; and v_p decreases at the outlet during outward expansion of the hump. We note that the velocities are not symmetric when the boundary is moving, unlike the symmetry seen when the boundary velocity is zero. This is due to the difference between the flow rate at inflow and outflow caused by mass conservation.

Figure 11 depicts snapshots of the axial velocity for Re = 800. We observe movement of the point of separation, which is indicated in the axial component of velocity by a change in

TABLE II
Error for Flow in Deforming Tube (Re = 200)

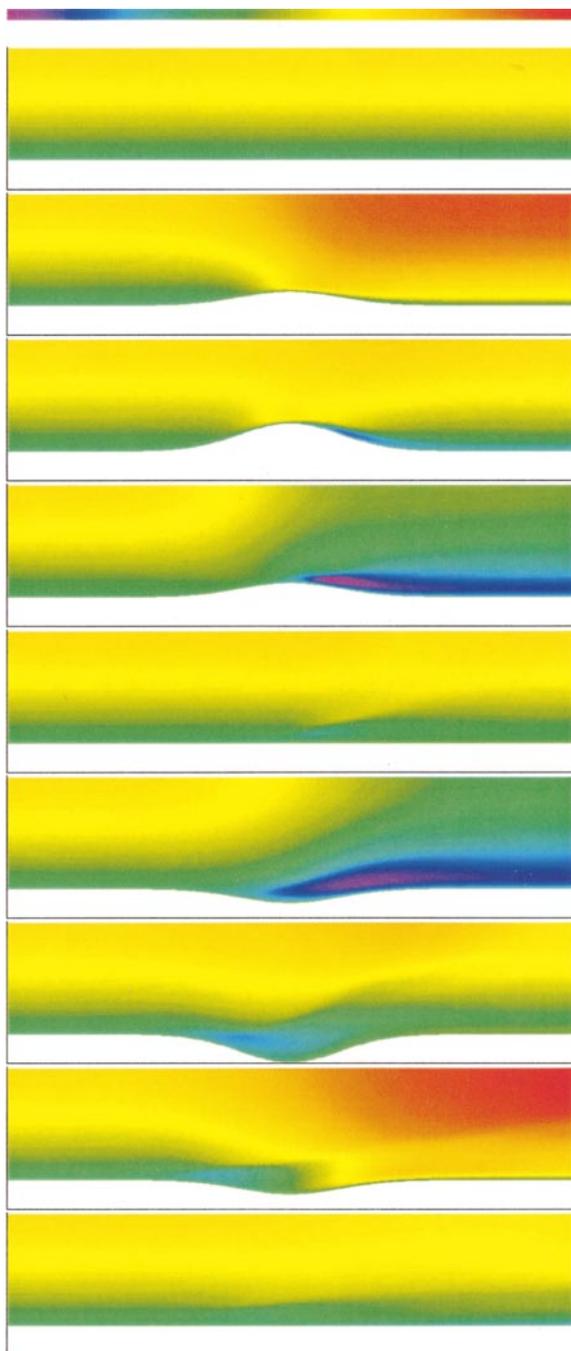| Case	$e^{1/16}$	Rate	$e^{1/32}$	Rate	$e^{1/64}$
u	2.71e-2	2.34	5.36e-3	1.94	1.40e-3
v	7.50e-2	2.39	1.43e-2	2.22	3.06e-3

FIG. 11. Axial velocity, v, at times $t = 0, 0.5, 1, 1.5, 2, 2.5; 3, 3.5, 4$ (inlet Re $= 800$). Tube wall moves from initial flat position at $t = 0$ to a fully pinched position at $t = 1$. It then moves outward past flat position at $t = 2$ to fully bulged position at $t = 3$ and returns to flat position at $t = 4$ after complete cycle. (Scale: -1.748 to 3.771.)
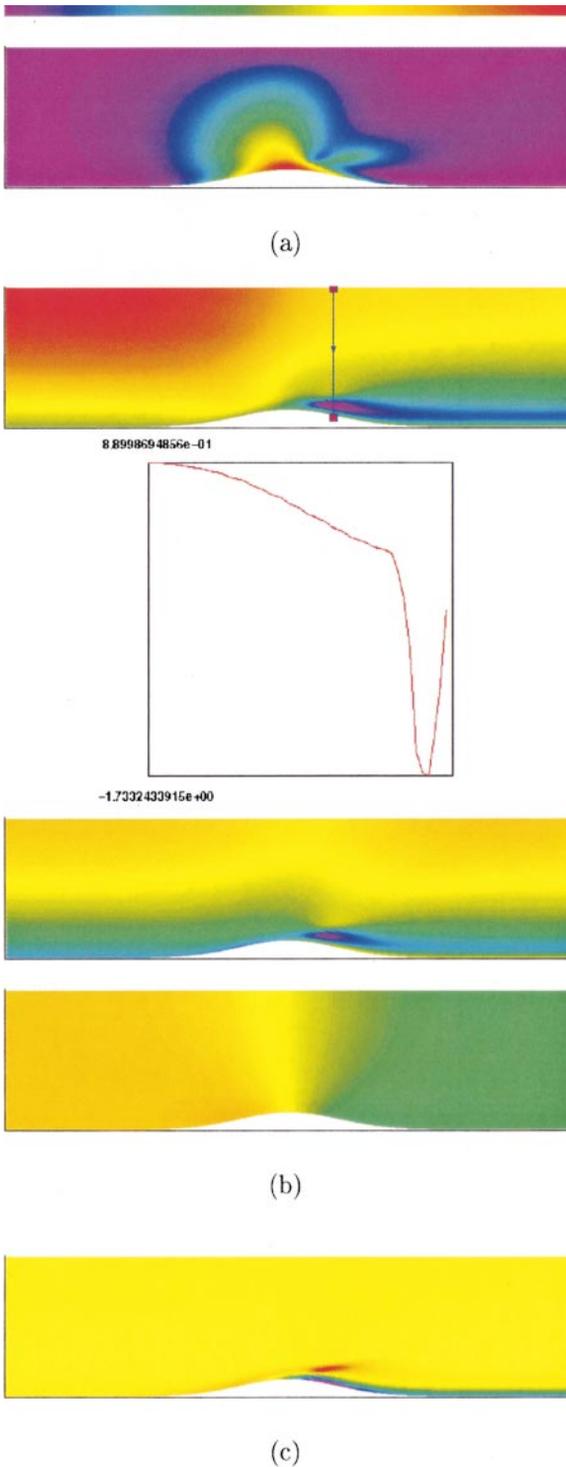
(a)

8.8998694856e-01

-1.7332433915e+00

(b)

(c)

FIG. 12. Deforming axisymmetric tube at $t = 1.5$ (inlet Re $= 800$). (a) Radial velocity, u. (Scale: -0.001 to 0.794). (b) Axial velocity, v, with slice through recirculation zone, and breakdown of vortical and potential components of axial velocity, v_v and v_p. (Scale: -1.748 to 2.000.) (c) Vorticity, ω. (Scale: -54.894 to 38.013.)

sign from positive to negative. As the hump expands outward, the separation point marches from a location before the midpoint of the hump toward the inlet. Another notable feature in this flow is a very sharp gradient which is captured in the axial component of the velocity at time $t = 3.5$, when the hump is moving back inward from its fully expanded outward position. The strong gradient, which indicates the presence of a shear layer, exists in the axial direction as well as the radial direction.

In Fig. 12 we show other fields for the Re $= 800$ flow at time $t = 1.5$. At this time the boundary is pulling back out from the fully pinched position. The wall is at its maximum velocity. Flow separation without reattachment is seen in the axial velocity and vorticity. We note the breakdown of axial velocity into its vortical and potential components. The flow is dominated near the boundary by the vortical component as it clearly captures the recirculation zone.

6. CONCLUSIONS

The article has presented an algorithm for incompressible, viscous flow in deforming domains based on an extension of the BCG predictor–corrector method. We have eliminated the complication of an inhomogeneous constraint by a split-velocity formulation. The splitting yields a potential flow problem with inhomogeneous boundary conditions for the divergence constraint and an evolution equation for the vortical component with time-dependent, but homogeneous, constraints. We have also presented a new time discretization for time-dependent, constrained systems. The algorithm produces results which are second-order accurate in space and time and can resolve time-dependent, separating flows.

The future of this work lies in geometry and boundary mechanics. The formulation applies equally well to other geometric descriptions. For example, the Cartesian grid embedded boundary method [3] can be extended as such, using the approach in [20] to treat viscous terms. Another desirable feature is a boundary which responds to the fluid pressure. Further coupling of the method to a structural solver would be a robust treatment of a fluid–solid interaction.

REFERENCES

1. A. Almgren, J. Bell, and W. Szymczak, A numerical method for the incompressible Navier–Stokes equations based on an approximate projection, *SIAM J. Sci. Comput.* **17**, 358 (1996).

2. A. Almgren, J. B. Bell, P. Colella, and L. H. Howell, A conservative adaptive projection method for the variable density incompressible Navier–Stokes equations, *J. Comput. Phys.* **142**(1), 1 (1998).

3. A. S. Almgren, J. B. Bell, P. Colella, and T. Marthaler, A Cartesian grid projection method for the incompressible Euler equations in complex geometries, *SIAM J. Sci. Comput.* **18**(5), 1289 (1997).

4. R. Aris, *Vectors, Tensors, and the Basic Equations of Fluid Mechanics* (Prentice Hall International, Englewood Cliffs, NJ, 1962).

5. R. Barrett, M. Berry, T. F. Chan, J. Demmel, J. Donato, J. Dongarra, V. Eijkhout, R. Pozo, C. Romine, and H. Van der Vorst, *Templates for the Solution of Linear Systems: Building Blocks for Iterative Methods* (SIAM, Philadelphia, 1994).

6. J. B. Bell, P. Colella, and H. M. Glaz, A second-order projection method for the incompressible Navier–Stokes equations, *J. Comput. Phys.* **85**, 257 (1989).

7. J. B. Bell, P. Colella, and L. H. Howell, An efficient second-order projection method for viscous incompressible flow, in *Proceedings of the Tenth AIAA Computational Fluid Dynamics, Conference, Honolulu, HI, June 24–26 1991* (American Institute of Aeronautics and Astronautics, New York, 1991), pp. 360–367.

8. J. B. Bell, P. Colella, J. A. Trangenstein, and M. Welcome, Adaptive mesh refinement on moving quadrilateral grids, in *Proceedings of the Ninth AIAA Computational Fluid Dynamics Conference, Buffalo, NY, June 14–16, 1989*, pp. 471.

9. J. B. Bell and W. B. Szymczak, Projection method for viscous incompressible flow on quadrilateral grids. *AIAA J.* **32**(10), 1961 (1994).

10. A. J. Chorin, Numerical solutions of the Navier–Stokes equations, *Math. Comput.* **22**, 745 (1968).

11. A. J. Chorin, On the convergence of discrete approximations to the Navier–Stokes equations, *Math. Comput.* **23**, 341 (1969).

12. P. Colella, Multidimensional upwind methods for hyperbolic conservation laws, *J. Comput. Phys.* **87**, 171(1990).

13. P. Colella and K. Pao, A projection method for low speed flows, *J. Comput. Phys.* **149**, 245 (1999).

14. P. Colella and D. P. Trebotich, Numerical simulation of incompressible viscous flow in deforming domains, *Proc. Natl. Acad. Sci. USA* **96**, 5378 (1999).

15. R. Cortez, An impulse-based approximation of fluid motion due to boundary forces, *J. Comput. Phys.* **123**, 341 (1996).

16. A. B. Downey, *Vigl 3.0: Visualization Graphics Library*, Technical Report UCB/CSD 95-000 (University of California, Berkeley, August 1995).

17. Y. C. Fung, *Foundations of Solid Mechanics* (Prentice Hall, New York, 1965).

18. F. Harlow and J. Welch, Numerical calculation of time-dependent viscous incompressible flow of fluids with free surfaces, *Phys. Fluids* **8**, 2182 (1965).

19. J. A. Hilditch, *A Projection Method for Low Mach Number Reacting Flow in the Fast Chemistry Limit*. Ph.D. thesis (University of California, Berkeley, 1997).

20. H. Johansen and P. Colella, A Cartesian grid embedded boundary method for Poisson's equation on irregular domains, *J. Comput. Phys.* **147**, 60 (1998).

21. R. Kupferman, Simulation of viscoelastic fluids: Couette–Taylor flow, *J. Comput. Phys.* **147**, 22 (1998).

22. M. Lai, *A Projection Method for Reacting Flow in the Zero Mach Number Limit*, Ph.D. thesis (University of California, Berkeley, 1994).

23. M. F. Lai, J. Bell, and P. Colella, A projection method for combustion in the zero Mach number limit, in *Proceedings of the Eleventh AIAA Computational Fluid Dynamics Conference* (American Institute of Aeronautics and Astronautics, New York, June 1993), pp. 776–783.

24. R. J. LeVeque, Immersed interface methods for Stokes flow with elastic boundaries or surface tension, *SIAM J. Sci. Comput.* **18**(3), 709 (1997).

25. M. L. Minion, On the stability of Godunov-projection methods for incompressible flow, *J. Comput. Phys.* **123**(2), 435 (1996).

26. P. Papadopoulos and R. L. Taylor, On the application of multi-step integration methods to infinitesimal elastoplasticity, *Int. J. Numer. Methods Eng.* **37**, 3169 (1994).

27. R. B. Pember, P. Colella, L. H. Howell, A. S. Almgren, J. B. Bell, W. Y. Crutchfield, V. E. Beckner, K. C. Kaufman, W. A. Fiveland, and J. P. Jessee, *The Modeling of a Laboratory Natural Gas-Fired Furnace with a Higher-Order Projection Method for Unsteady Combustion*, Technical Report UCRL-JE-123244 (Lawrence Livermore National Laboratory, February 1996). [Presented at the Twenty-Sixth International Symposium on Combustion, Naples, Italy, July 28–Aug. 2, 1996]

28. C. S. Peskin and D. M. McQueen, Cardiac fluid dynamics, *Crit. Rev. Biomed. Eng.* **20**(5–6), 451 (1992).

29. L. Petzold, Recent developments in the numerical solution of differential/algebraic systems. *Comput. Methods Appl. Mech. Eng.* **48**, 77 (1989).

30. M. M. Sussman, A. Almgren, J. B. Bell, P. Colella, L. H. Howell, and M. Welcome, An adaptive level set approach for incompressible two-phase flows, *J. Comput. Phys.* **148**, 81 (1999).

31. D. P. Trebotich, *A Projection Method for Incompressible Viscous Flow on a Deformable Domain* Ph.D. thesis (University of California, Berkeley, 1998).